Supplementary Information

Singe atom Bi decorated copper alloy enables C-C coupling for electrocatalytic reduction of CO_2 into C_{2+} products

Authors:

Yucheng Cao[1,2,7], Suya Chen[3,7], Shuowen Bo[4,7], Wenjun Fan[1], Jiangnan Li[1,2], Chunmei Jia[1], Zhen Zhou[3,5], Qinghua Liu[4], Lirong Zheng[6] and Fuxiang Zhang[*1]

Affiliations:

[1] State Key Laboratory of Catalysis, Dalian Institute of Chemical Physics, Chinese Academy of Sciences, Dalian National Laboratory for Clean Energy, Dalian 116023, Liaoning, China.

[2] Center of Materials Science and Optoelectronics Engineering, University of Chinese Academy of Sciences; Beijing 100049, China.

[3] School of Materials Science and Engineering, Institute of New Energy Material Chemistry, Renewable Energy Con-version and Storage Center (ReCast), Key Laboratory of Advanced Energy Materials Chemistry (Ministry of Educa-tion), Nankai University, Tianjin 300350, China.

[4] National Synchrotron Radiation Laboratory, University of Science and Technology of China, Hefei 230029, Anhui, China.

[5] School of Chemical Engineering, Zhengzhou University, Zhengzhou 450001, Henan, China.

[6] Beijing Synchrotron Radiation Facility, Institute of High Energy Physics, Chinese Academy of Sciences, Beijing 100049, China.

[7] These authors contributed equally: Yucheng Cao, Suya Chen, Shuowen Bo.

[*]Correspondence to: fxzhang@dicp.ac.cn

Supplementary methods

DFT calculation details

The binding strength of different Configurations for the BiCu-SAA catalyst was evaluated by the binding energy (Eb), which is defined as:

$$E_b = E_{BiCu(111)\text{-}SAA} - E_{Cu(111)} - E_{Bi} \quad (1)$$

where the $E_{BiCu(111)\text{-}SAA}$ is the total energy of the catalyst system, $E_{Cu(111)}$ represents the energy of the system without a supported or embedded Bi atom, and E_{Bi} represents the energy of a single Bi atom in vacuum. In general, when E_b is more negative, the catalyst is thermodynamically more stable. The exact reaction conditions for different catalysts were shown in Supplementary Fig. 25 and Supplementary Table 3.

The lattice parameter of the optimized Cu(111) slab was 3.63 Å, which was very close to the experimental lattice parameter of 3.62 Å. The Cu(111) slab was composed of three layers (the top layer was allowed to relax and the bottom two layers were fixed to the bulk Cu configuration). The optimized structures of the key intermediates within CO_2 reduction to C_2H_4 on Cu(111) and BiCu(111)-SAA surfaces were displayed in Supplementary Fig. 26 and Fig. 27.

The catalytic activity of the studied catalysts was calculated by the computational hydrogen electrode (CHE) model[1]. The free energy change of each elementary step was determined as:

$$\Delta G = \Delta E + \Delta ZPE - T\cdot\Delta S \quad (2)$$

where ΔE, ΔZPE, and $T\cdot\Delta S$ represent the reaction energy, the zero-point energy correction change, and the change in entropy contribution. The free energy correction was performed by the VASPKIT code[2].

The charge density difference for the BiCu(111)-SAA slab was calculated according to:

$$\Delta\rho = \rho_{BiCu(111)\text{-}SAA} - (\rho_{Bi} + \rho_{Cu(111)}) \quad (3)$$

where $\rho_{BiCu(111)\text{-}SAA}$ is the charge density of the whole system, ρ_{Bi} is the charge density of a single Bi atom, and $\rho_{Cu(111)}$ is the charge density of the BiCu(111)-SAA system after removing the embedded Bi.

Evaluation of CO_2RR performance

For gaseous products, the Faradaic efficiency (FE) was calculated as:

$$FE_a\ (\%) = i_a/i_{total} \times 100\% = x_a \times f_{CO2} \times N_a \times F/i_{total} \times 100\% \quad (4)$$

where i_a is the partial current towards species a (A), i_{total} is the total current (A), x_a is the concentration of species a measured by GC (mol mol^{-1}), f_{CO2} is the CO_2 flow rate (mol s^{-1}), N_a is the number of exchanged electrons to produce species g from CO_2, and F is Faraday constant (96485 C mol^{-1}).

For liquid products, the Faradaic efficiency (FE) was calculated as:

$$FE_b\ (\%) = q_b/q_{total} \times 100\% = F \times c_b \times V \times N_b/q_{total} \times 100\% \quad (5)$$

where q_b is the partial charge to produce species b (C), q_{total} is the total charge passed (C), V is the electrolyte volume (L), and c_b is the concentration of species b calculated from the ^1H NMR with internal standard method (mol L^{-1}).

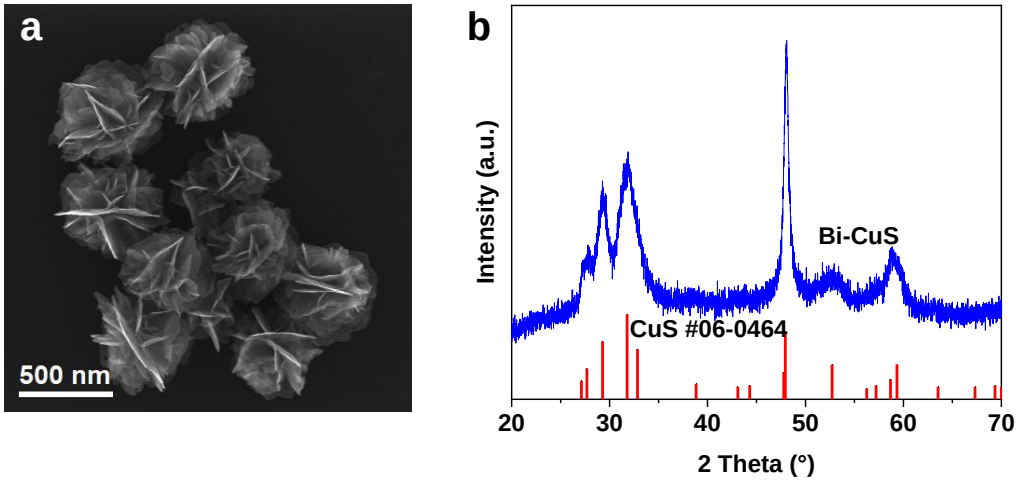

Supplementary Fig. 1 | Structural characterizations of Bi-CuS precursor: (a) SEM image; (b) XRD patterns.

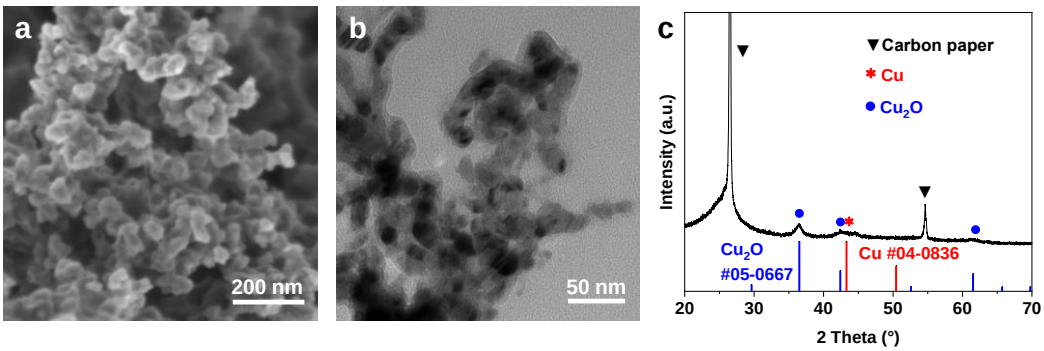

Supplementary Fig. 2 | Structural characterizations of Cu-Nano catalyst prepared: (a) SEM image, (b) TEM image, (c) XRD patterns.

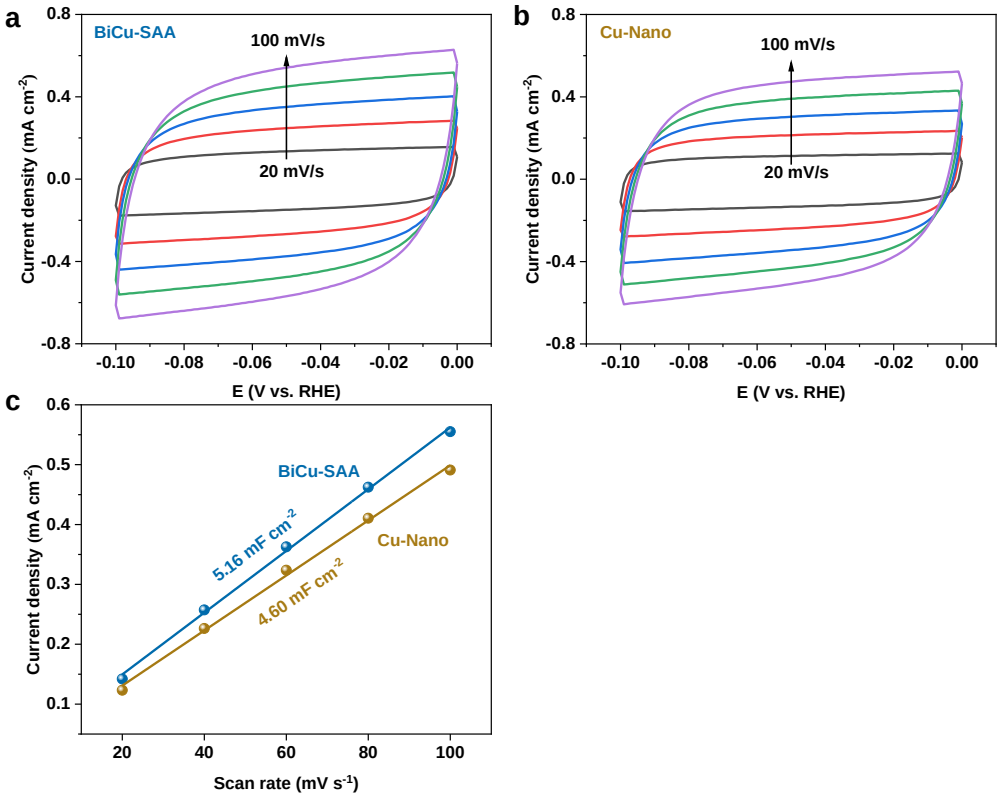

Supplementary Fig. 3 | CV curves of the BiCu-SAA **(a)** and Cu-Nano catalysts **(b)** obtained in capacitance region at varying scan rate, and their corresponding capacitance current density at -0.05 V vs. RHE as a function of scan rate **(c)**.

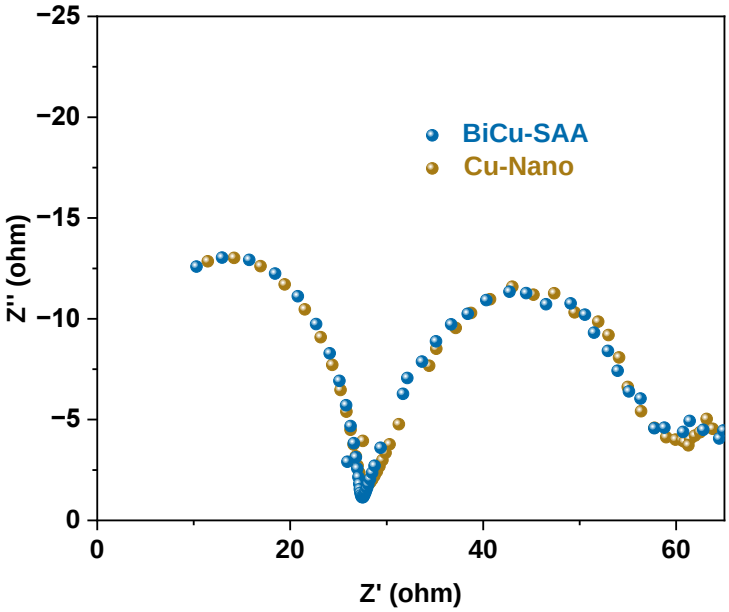

Supplementary Fig. 4 | Electrochemical impedance spectroscopy (EIS) of the BiCu-SAA and Cu-Nano catalysts at the applied potential of -0.8 V vs. RHE.

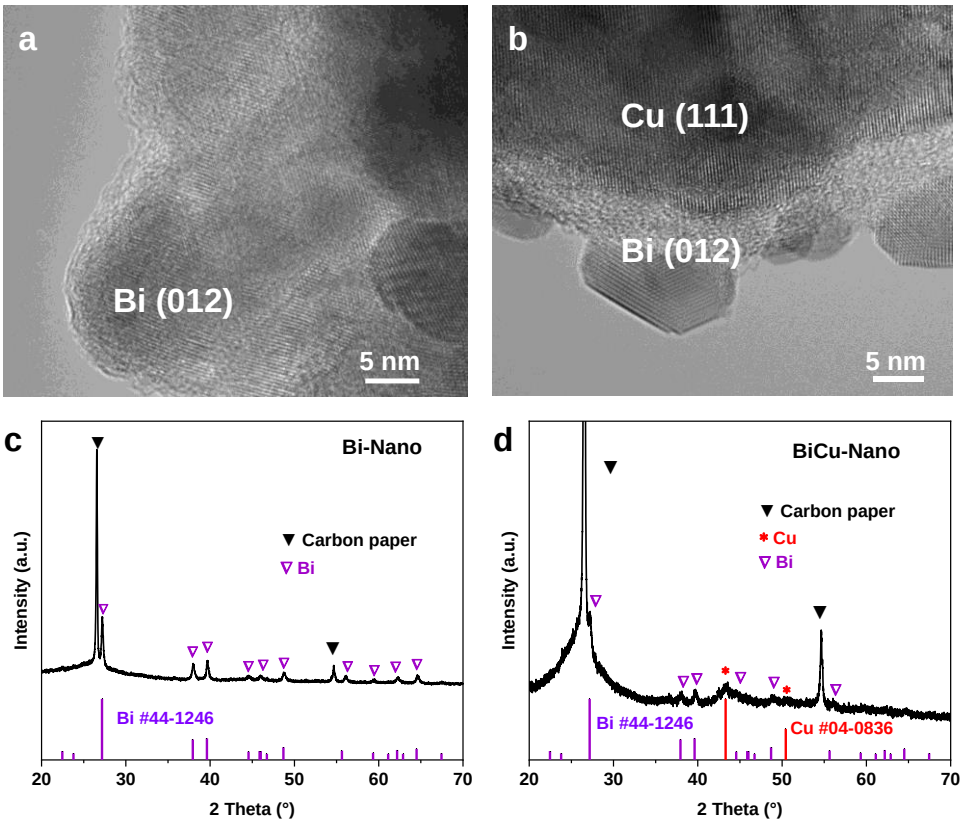

Supplementary Fig. 5 | Structural characterizations of Bi-Nano (a, c) and BiCu-Nano (b, d) catalysts: (a, b) HR-TEM images; (c, d) XRD patterns.

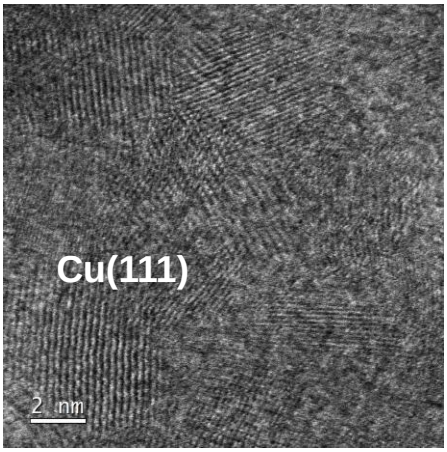

Supplementary Fig. 6 | HAADF-STEM image of the BiCu-SAA in the bright field corresponding to Fig. 1a, where the Cu(111) facet can be recognized.

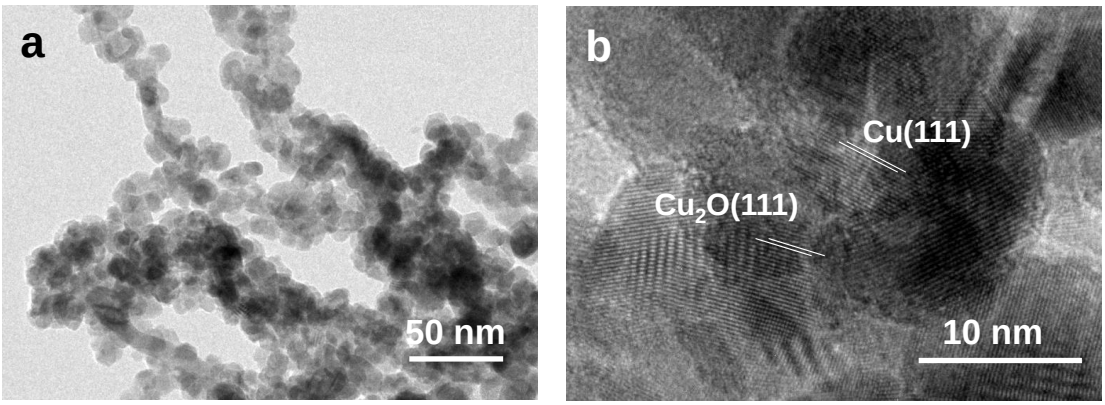

Supplementary Fig. 7 | HRTEM images of the BiCu-SAA catalyst.

Note: It shows the completely different morphology from the nanoflower of its precursor Bi-CuS, indicating the structural reconstruction of Bi-CuS complex precursors during the electroreduction treatment. Meanwhile, Cu(111) and Cu_2O(111) facet can be clearly observed.

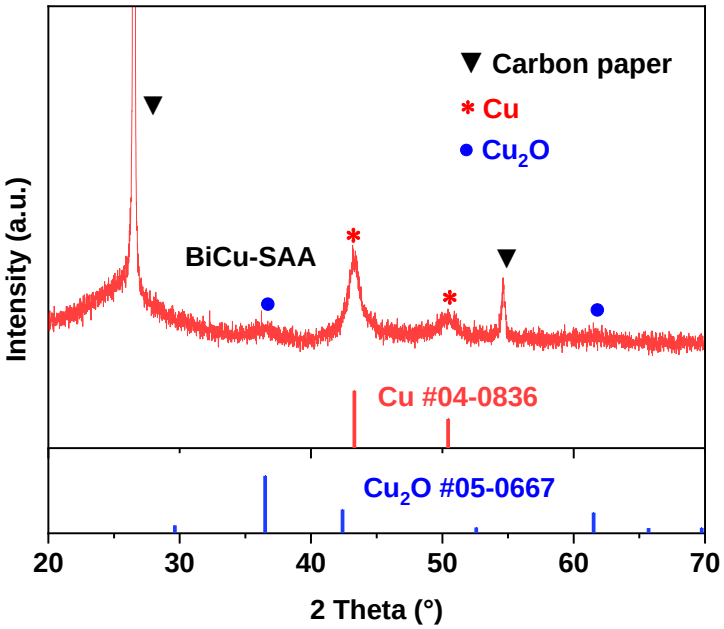

Supplementary Fig. 8 | XRD pattern of the BiCu-SAA catalyst.

Note: Both Cu and Cu_2O phases can be detected but without the presence of CuS and Bi nanoparticle species, ruling out the existence of Bi nanoparticles.

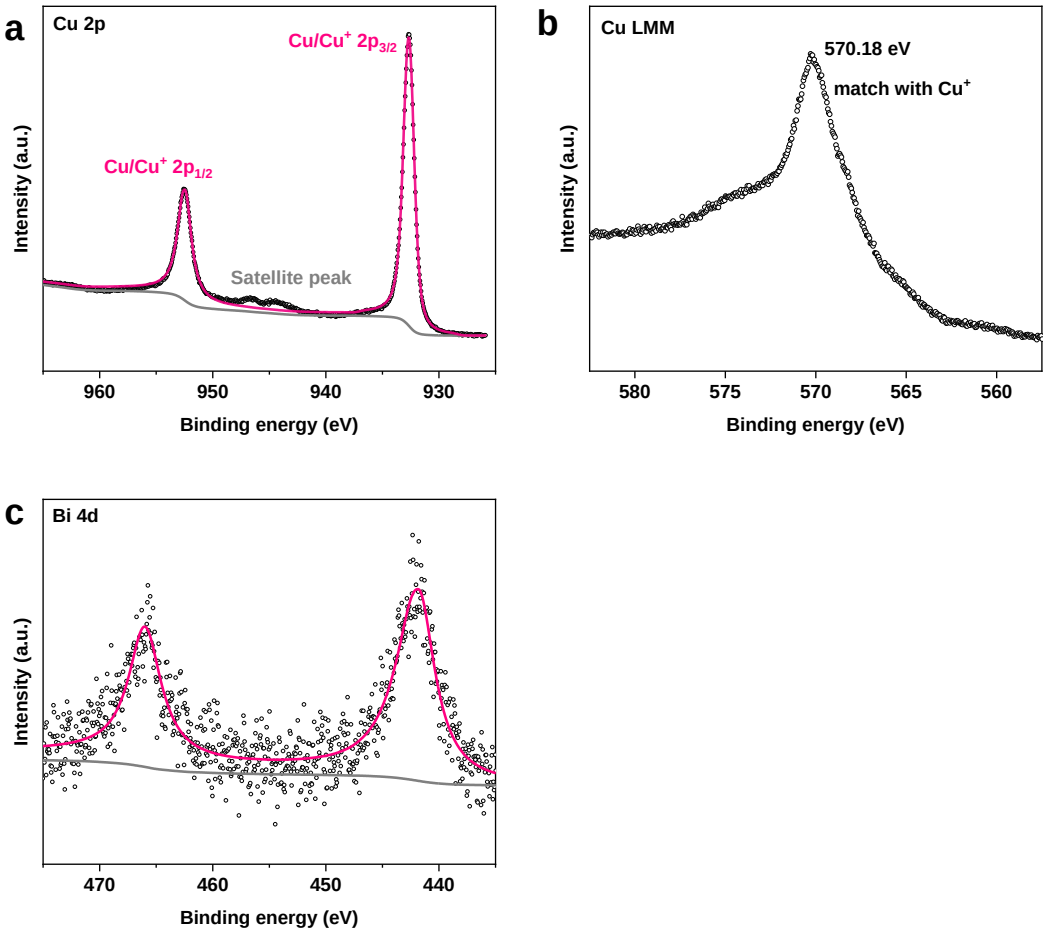

Supplementary Fig. 9 | XPS spectra of the BiCu-SAA catalyst: (a) Cu 2p spectrum, (b) Cu LMM spectrum, (c) Bi 4d spectrum.

Note: Based on the Cu LMM spectrum, the Cu^{+} valence state can be detected and confirmed, revealing the part oxidation of Cu nanoparticle during exposure to air. Meanwhile, the presence of bismuth on the surface can be demonstrated by the Bi 4d spectrum.

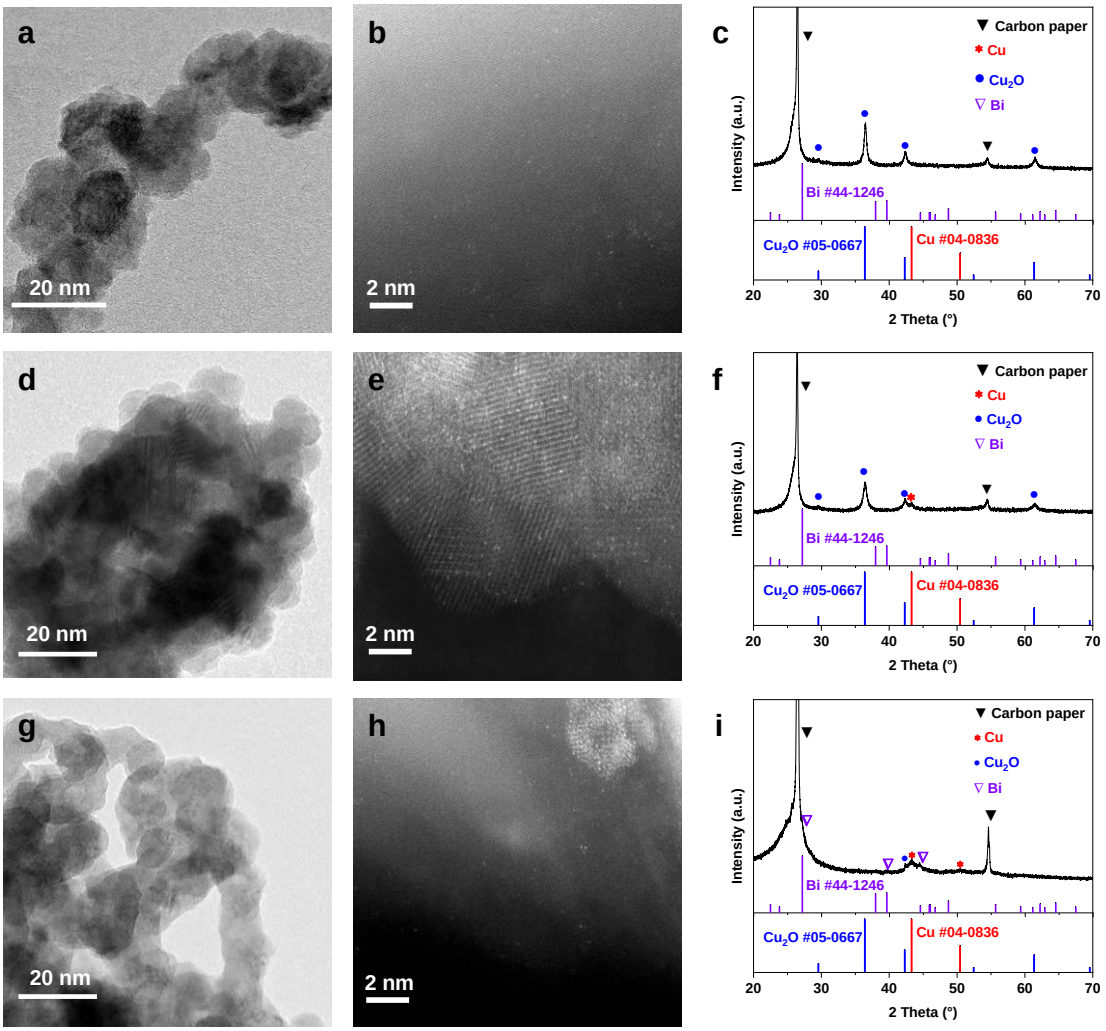

Supplementary Fig. 10 | HR-TEM images **(a, d, g)**, HADDF-STEM images **(b, e, h)** and XRD patterns **(c, f, i)** of the BiCu-SAA catalysts with Bi content of 2.2 wt%, 6.5 wt% and 15.6 wt%, respectively.

Note: The above characterization results validate the formation of single atomic dispersion of Bi on the Cu when Bi content is not higher than 6.5 wt%, and the coexistence of Bi nanoparticles and single atoms is observed for the sample with Bi content of 15.6 wt%.

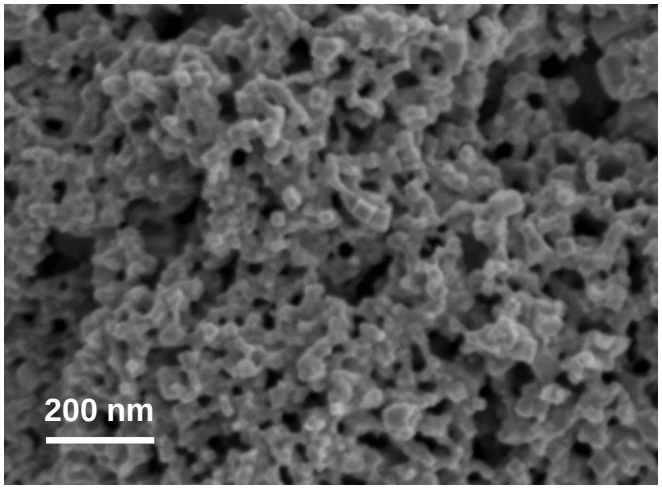

Supplementary Fig. 11 | SEM image of the BiCu-SAA catalyst.

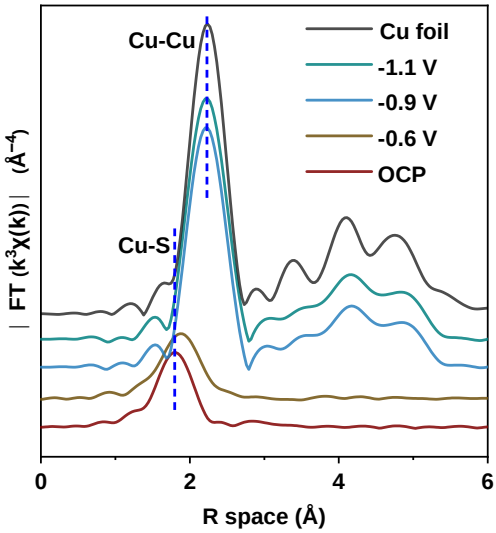

Supplementary Fig. 12 | Fourier transform curves of in-situ EXAFS data at Cu K-edge for the BiCu-SAA catalyst.

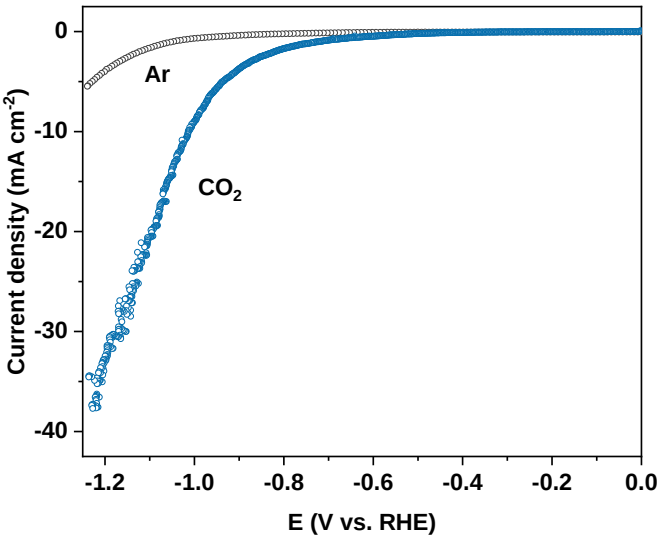

Supplementary Fig. 13 | LSV curves of the BiCu-SAA catalyst obtained at the scan rate of 10 mV s^{-1} in an H-type cell under CO_2 and Ar flow, respectively.

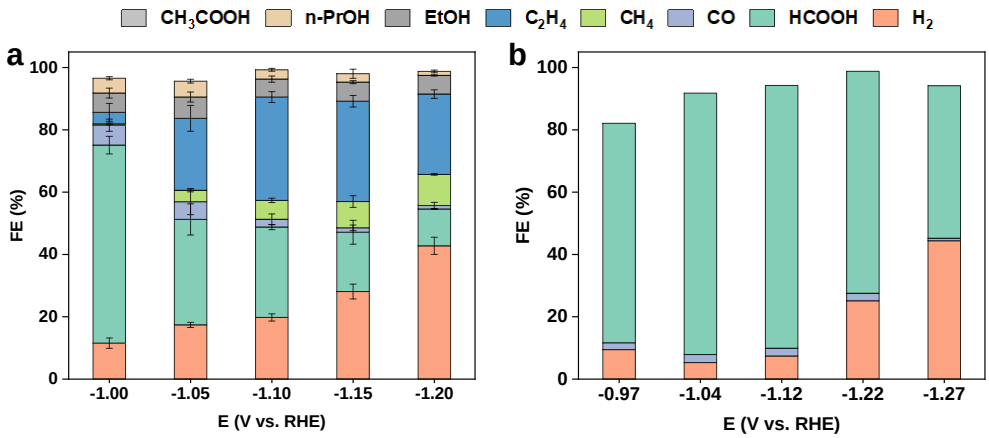

Supplementary Fig. 14 | The FEs of CO_2RR products on the control samples obtained at different applied potentials: (a) Cu-Nano; (b) Bi-Nano.

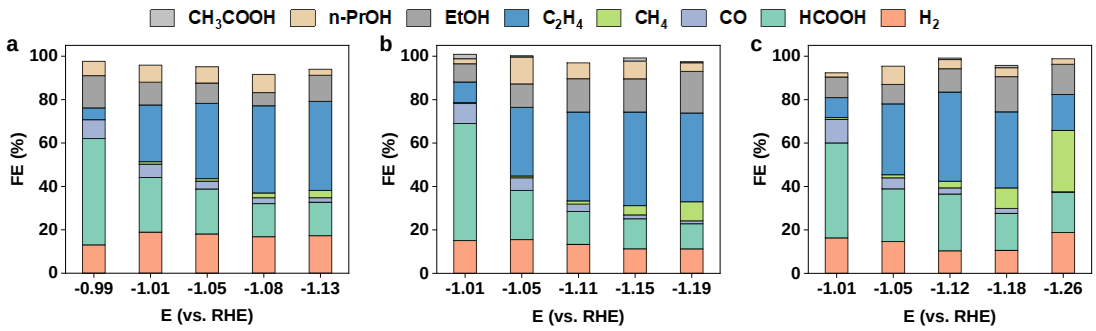

Supplementary Fig. 15 | The FEs of CO_2RR products on the BiCu-SAA catalysts with different Bi content obtained at different applied potentials: (a) 2.2 wt%, (b) 6.5 wt%, (c) 15.6 wt%.

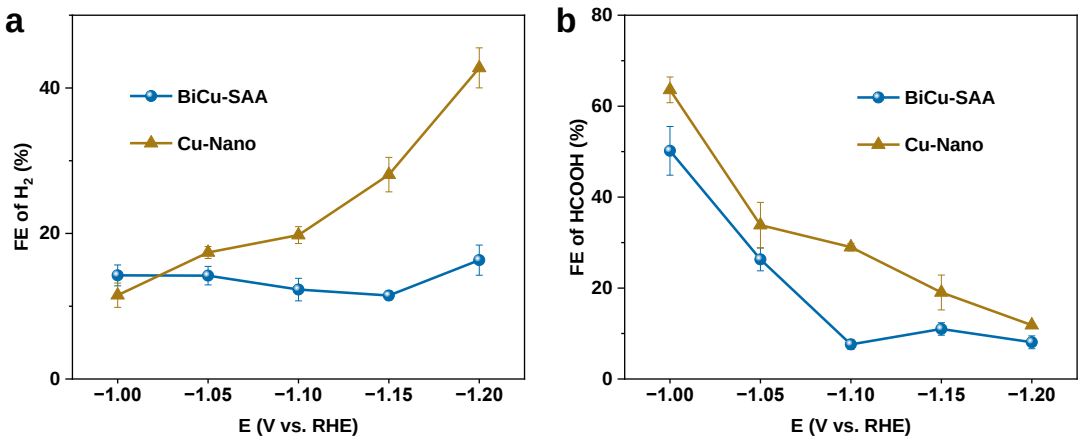

Supplementary Fig. 16 | The FEs of H_2 **(a)** and HCOOH **(b)** on the BiCu-SAA and Cu-Nano catalysts obtained at different applied potentials.

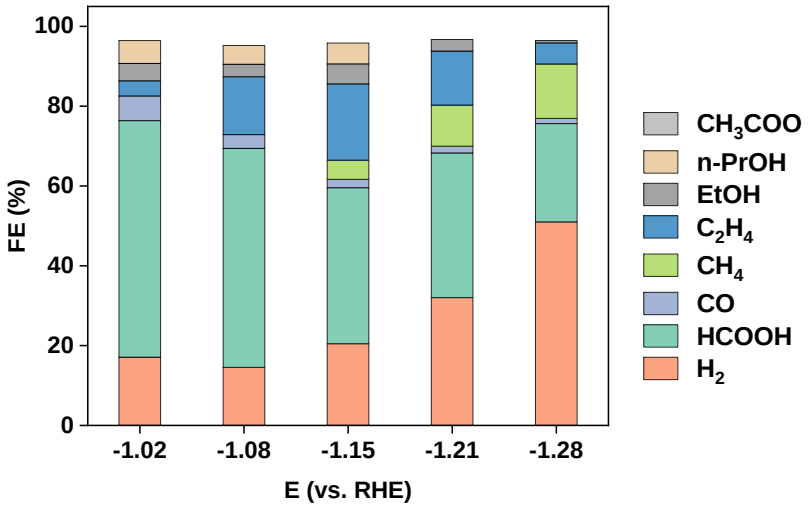

Supplementary Fig. 17 | The FEs of CO_2RR products on the BiCu-Nano catalyst obtained at different applied potentials.

Note: It exhibits even more inferior FEs for the C_{2+} products with respect to the Cu-Nano catalyst, as should result from partial coverage of loaded Bi on the Cu active sites.

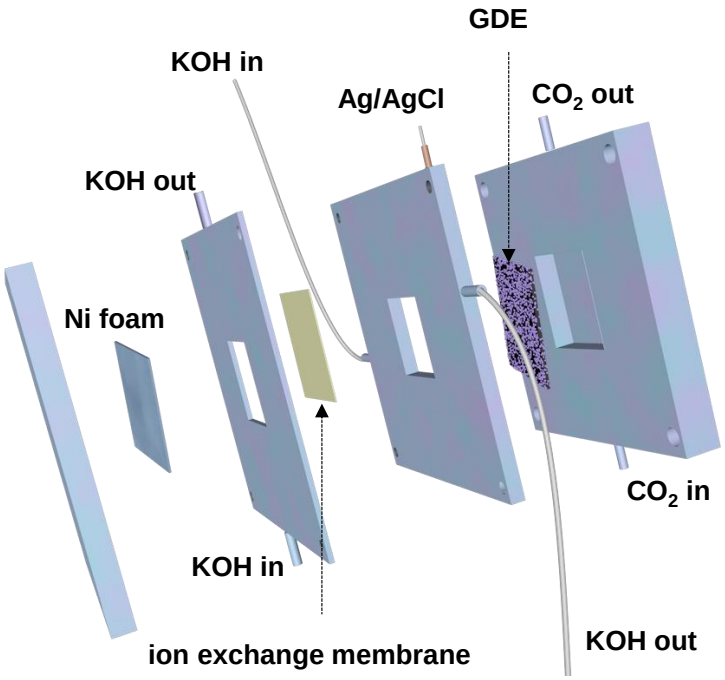

Supplementary Fig. 18 | Schematic diagram of the flow-cell for CO_2RR.

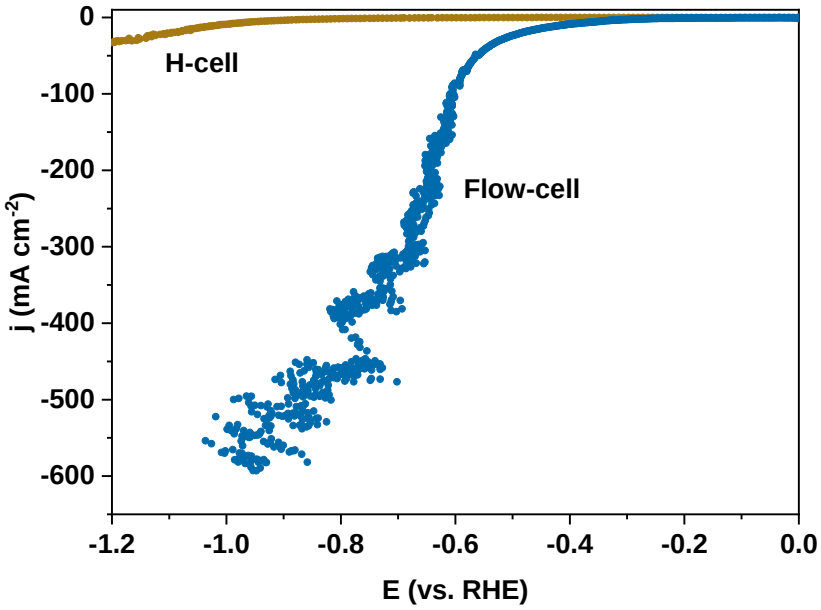

Supplementary Fig. 19 | LSV curves of CO_2RR in the H-type cell and the flow-cell. Note: The scan rate is 10 mV s^{-1}. The polarization response curve in the flow cell shows a significant improvement in current density with respect to the H-type cell, as can be attributed to enhanced CO_2 mass transport at the three-phase interfaces and the catalytic promotion effect of hydroxide ions.

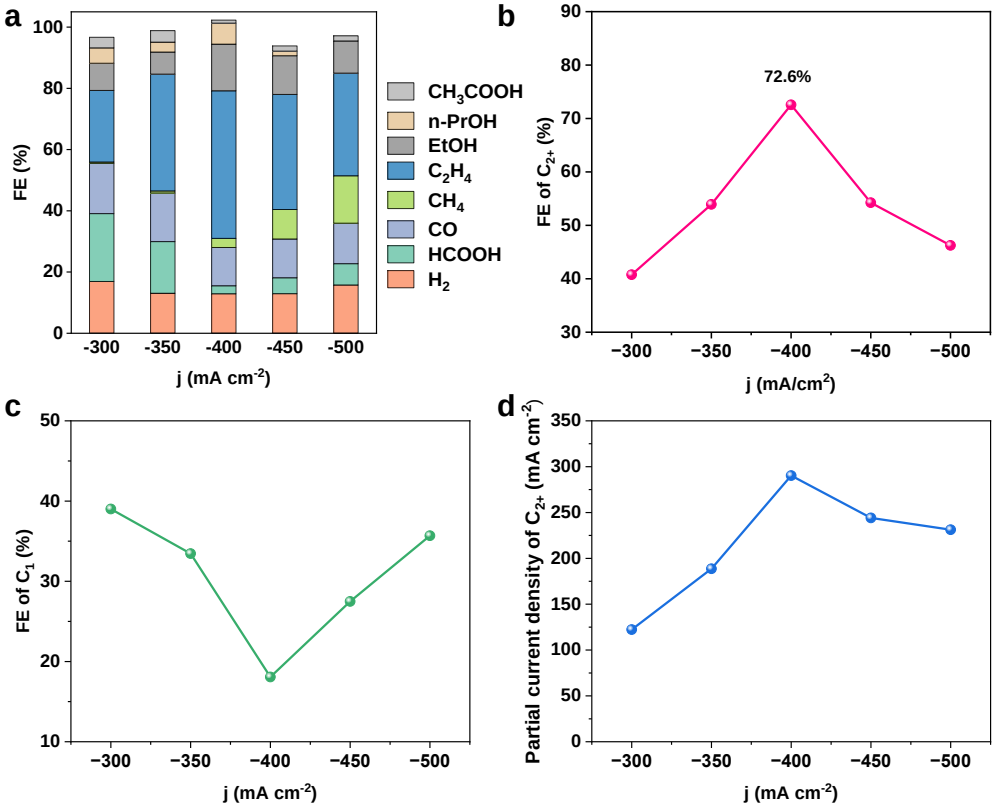

Supplementary Fig. 20 | Performance of CO_2RR on the BiCu-SAA in the flow-cell as a function of current density. (a) FEs values of various products, (b) FEs of C_{2+} products, (c) FEs of C_1 products, (d) The partial current density of C_{2+} products.

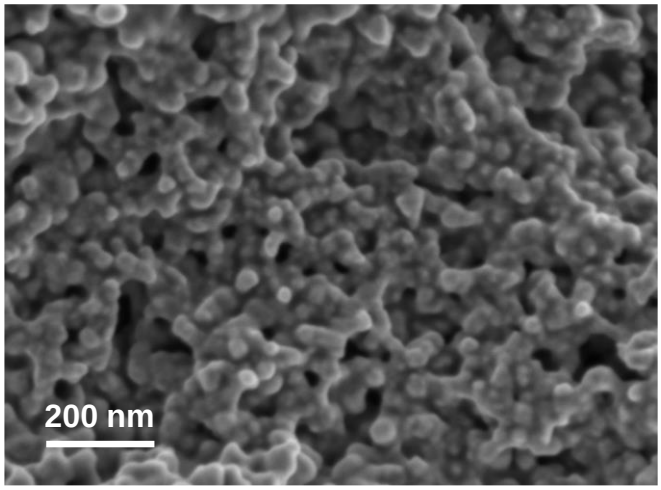

Supplementary Fig. 21 | SEM image of the BiCu-SAA catalyst after stability test.

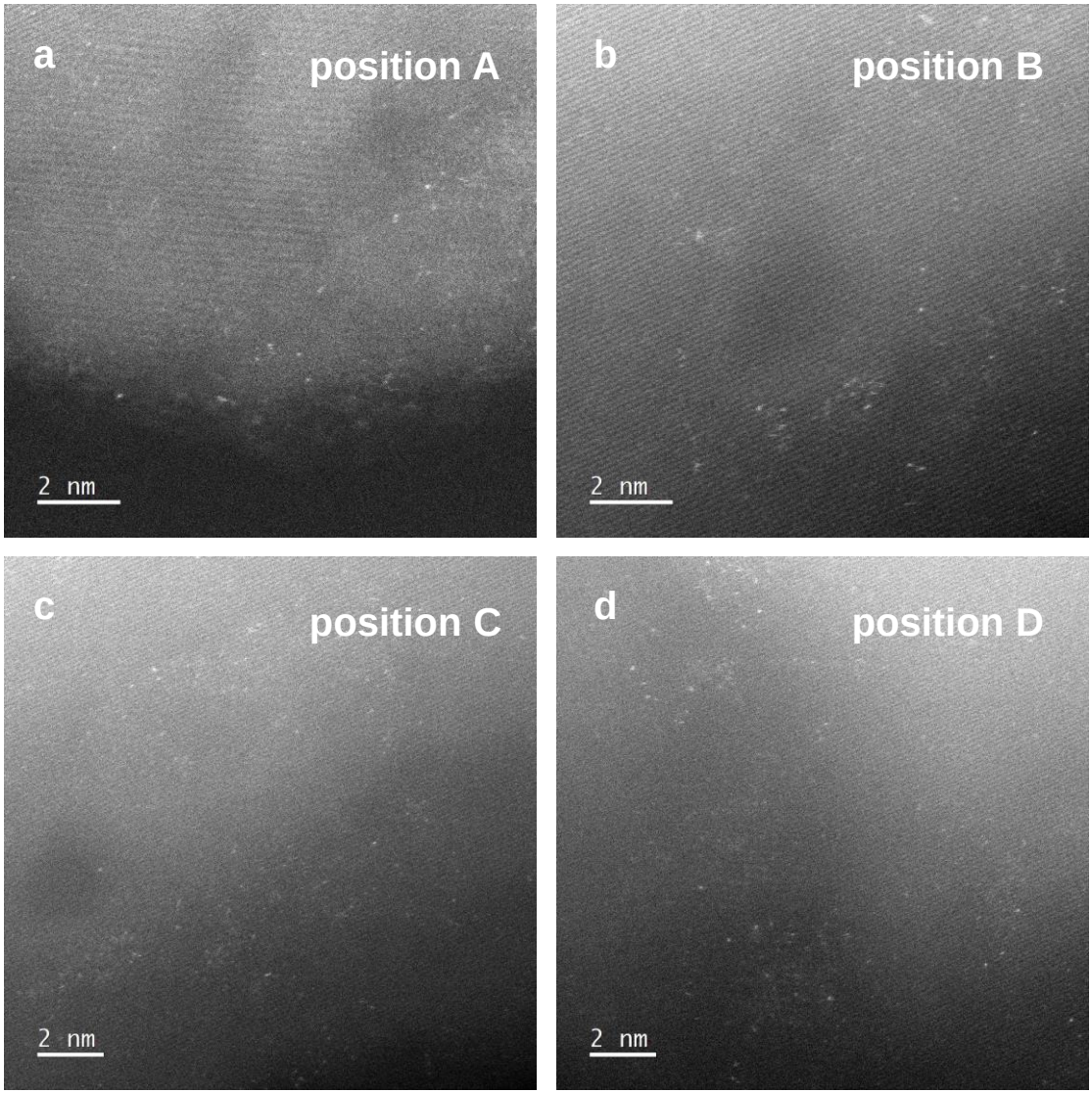

Supplementary Fig. 22 | HADDF-STEM images obtained at different positions of the BiCu-SAA catalyst after stability test.

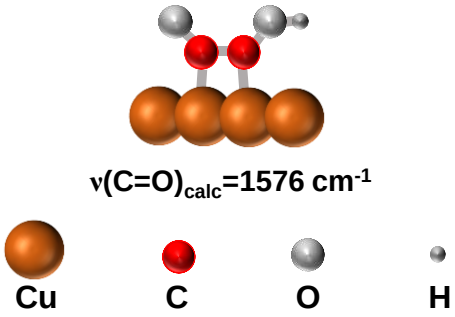

Supplementary Fig. 23 | The calculated (calc) harmonic vibrational frequencies of the C=O stretching vibration in the *COCOH intermediates on the Cu adsorption sites.

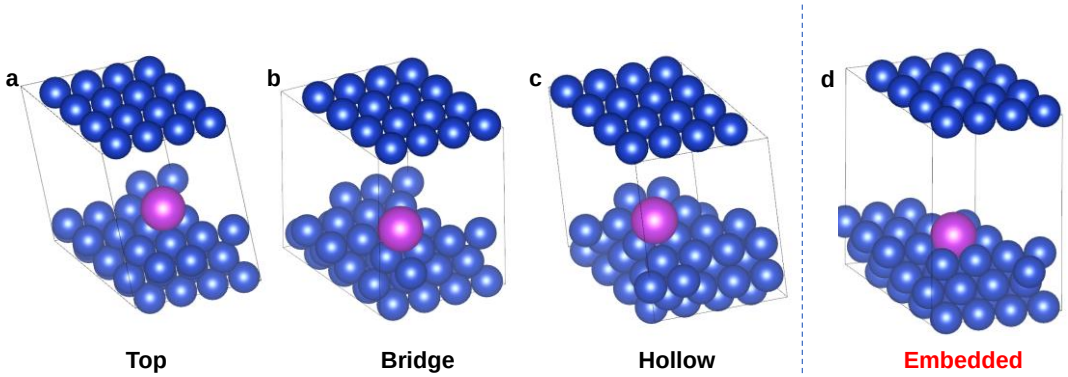

Supplementary Fig. 24 | Different configuration of Bi atom on Cu(111) slab. **a, b, c,** Bi supported on the Cu(111) surface. **d,** Bi embedded in the Cu(111) surface. (Cu, blue; Bi, purple).

Note: By calculating the binding energy, the Bi atom was more inclined to be embedded in the Cu(111)-Nano rather than supported on the Cu(111)-Nano surface, which is consistent with the HAADF-STEM result. Thus, the configuration of Bi embedded in Cu(111)-Nano slab was used for DFT calculations.

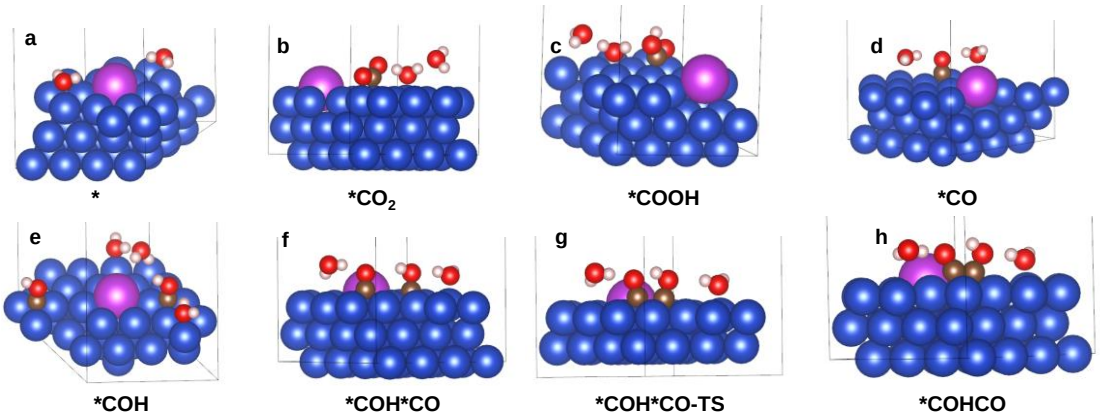

Supplementary Fig. 25 | The optimized structures of the key intermediates on the BiCu(111)-SAA slab. Cu, blue; Bi, purple; C, golden; O, red; H, white.

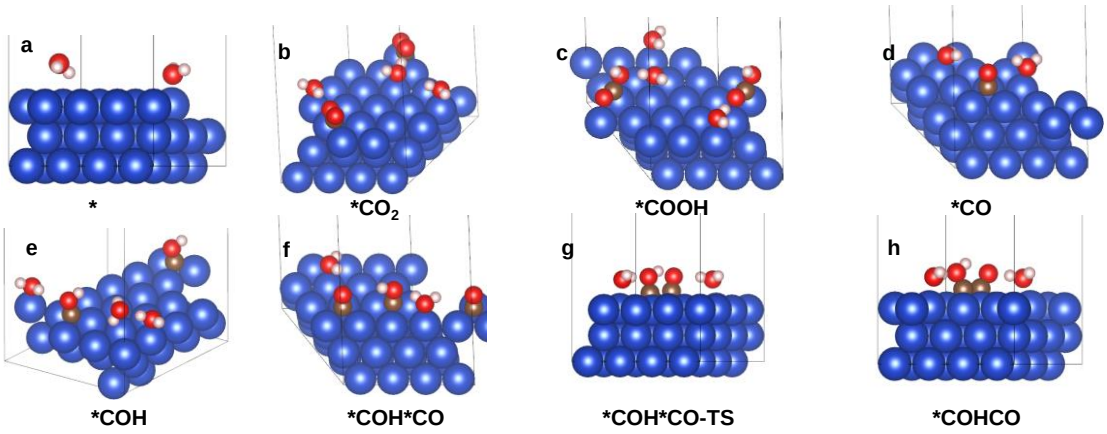

Supplementary Fig. 26 | The optimized structures of the key intermediates on the Cu(111)-Nano slab. Cu, blue; C, golden; O, red; H, white.

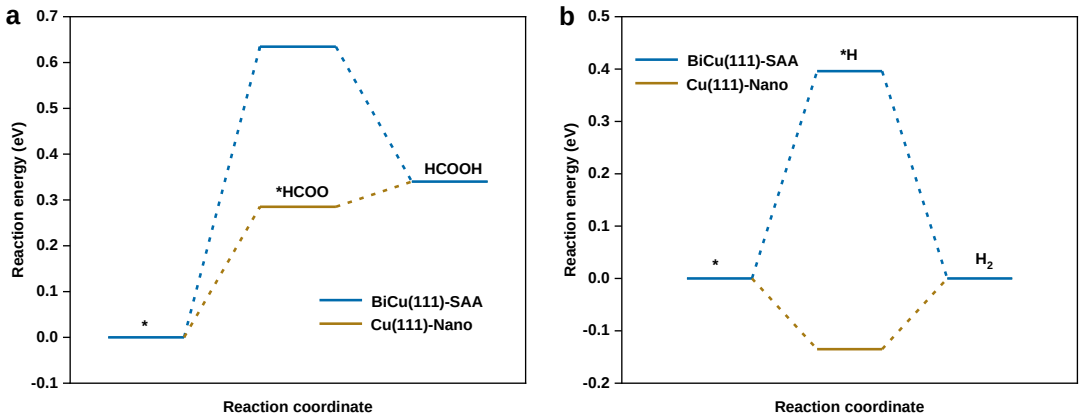

Supplementary Fig. 27 | The reaction energy diagram for the CO_2RR to formate **(a)** and HER **(b)** on the BiCu(111)-SAA and Cu(111)-Nano.

Supplementary Table 1 | Electrocatalytic performances for CO_2RR over Cu-based single atom catalysts reported recently

Catalyst	Electrocatalytic Cell	Electrolyte	Main product	FE	Ref.
BiCu-SAA	H-cell	0.1 M $KHCO_3$	C_2H_4	73.4% (C_{2+})	This work
	Flow-cell	1.0 M KOH	C_2H_4	72.6% (C_{2+})	
$Cu_{97}Sn_3$	H-cell	0.5 M $KHCO_3$	CO	CO (98%)	Ref [3]
Pb_1Cu	Flow-cell	0.5 M $KHCO_3$	HCOOH	HCOOH (96%)	Ref [4]
Sn-CuO	H-cell	Ionic liquid	MeOH	MeOH (88.6%)	Ref [5]
Bi-Pd SAA	H-cell	0.5 M $KHCO_3$	CO	CO (90.5%)	Ref [6]
Cu_1Au	H-cell	0.1 M $KHCO_3$	CO	CO (95%)	Ref [7]
AgCu SAA	H-cell	0.1 M $KHCO_3$	CO	CO (97.5%)	Ref [8]

Supplementary Table 2 | The exact reaction conditions for different catalysts

Bi content (wt%)	$CuTuCl \cdot 0.5H_2O$ (mg)	$Bi(DDTC)_3$ (mg)	EG (mL)	Temperature (℃)	Time (h)
0	50	0	40	120	2
2.2	50	30	40	120	1.5
3.7	50	30	40	120	2
6.5	50	50	40	120	2
15.6	50	30	40	120	4
100	0	30	40	120	3

Supplementary Table 3 | The exact reaction conditions for different catalysts

Configuration	Binding energy (eV)
top	-4.418
bridge	4.417
hollow	-4.445
embedded	-5.670

Supplementary References

1. Nørskov, J. K. et al. Origin of the overpotential for oxygen reduction at a fuel-cell cathode. *J. Phys. Chem. B* **108**, 17886-17892 (2004).
2. Wang, V. et al. Vaspkit:A user-friendly interface facilitating high-throughput computing and analysis using vasp code. *Comput. Phys. Commun.* **267**, 108033 (2021).
3. Ren, W. et al. Isolated copper-tin atomic interfaces tuning electrocatalytic CO_2 conversion. *Nat. Commun.* **12**, 1449 (2021).
4. Zheng, T. et al. Copper-catalysed exclusive CO_2 to pure formic acid conversion via single-atom alloying. *Nat. Nanotechnol.* **16**, 1386-1393 (2021).
5. Guo, W. et al. Highly efficient CO_2 electroreduction to methanol through atomically dispersed Sn coupled with defective CuO catalysts. *Angew. Chem. Int. Ed.* **60**, 21979-21987 (2021).
6. Xie, H. et al. Boosting Pd-catalysis for electrochemical CO_2 reduction to CO on Bi-Pd single atom alloy nanodendrites. *Appl. Catal. B Environ.* **289**, 119783 (2021).
7. Zhao, Y. et al. Atomic-level-designed copper atoms on hierarchically porous gold architectures for high-efficiency electrochemical CO_2 reduction. *Sci. China Mater.* **64**, 1900-1909 (2021).
8. Wang, H. et al. Surface restructuring in AgCu single-atom alloy catalyst and self-enhanced selectivity toward CO_2 reduction. *Electrochim. Acta* **426**, 140774 (2022).